PAPER • OPEN ACCESS

Acoustic transport in higher-order topological insulators with Dirac hierarchy

View the article online for updates and enhancements.

New Journal of Physics

The open access journal at the forefront of physics

PAPER

CrossMark

Acoustic transport in higher-order topological insulators with Dirac hierarchy

Xinglong Yu[1], Xin Zhang[1,2,*], Li Luo[1], Licheng Wang[1], Jiebin Peng[1], Yingyi Huang[1], Yuan Guo[1], Jing Cai[1], Yanping Wang[1], Degang Zhao[3], Yuanwei Yao[1] and Fugen Wu[2]

1   School of Physics and Optoelectronic Engineering, Guangdong University of Technology, Guangzhou 510006, People's Republic of China
2   School of Materials and Energy, Guangdong University of Technology, Guangzhou 510006, People's Republic of China
3   School of Physics, Huazhong University of Science and Technology, Wuhan 430074, People's Republic of China
*   Author to whom any correspondence should be addressed.

E-mail: xinxintwinkle@163.com

Keywords: acoustic transport, Dirac hierarchy, three-dimensional higher-order topological insulators

Supplementary material for this article is available online

Abstract

Dirac cones (DCs) are an important band structure in topological insulators (TIs) for realizing topological phase transition, and they provide unique ways to artificially regulate wave transport. Herein, we proposed a simple method to achieve Dirac hierarchy in three-dimensional (3D) acoustic TIs with rich and controllable topological phase transitions. The split of multifold DCs in each bulk Dirac hierarchy induced boundary Dirac hierarchy, including topological surface states and topological hinge states. We successfully realized 3D higher-order topological insulators (HOTIs) that exhibited two-fold boundary Dirac hierarchy with hinge states and achieved energy transport along three independent directions based on hinge-to-hinge channels. The proposed method is not limited to single hinges, and it provides a new design idea for multidimensional sound transport, serving as the basis for controllable acoustic functional devices.

1. Introduction

The discovery of topological insulators (TIs) has provided novel opportunities for advances in the research on condensed matter physics and material science [1–15]. The concept of higher-order topological insulators (HOTIs)—a new category of TIs—originated from quantum electronic systems [16–18]. The topological properties of HOTIs are characterized by fractional bulk polarization, which sets them apart from traditional TIs characterized by integral topological invariants. Contemporary research has shown that HOTIs exhibit extended bulk-boundary correspondence, with the nth-order TIs possessing $(D–n)$-dimensional topological boundary states in a D-dimensional system [16, 19–25]. For instance, a three-dimensional (3D) first-order TI contains two-dimensional (2D) topological surface states within the bulk bandgap, while a 3D second-order TI features one-dimensional (1D) topological hinge states [26, 27]. In particular, the hinge states in 3D second-order TIs are localized at the hinges of the system, and they exhibit novel transfer characteristics [28–35]. Initially proposed in condensed matter systems, 3D HOTIs can efficiently manipulate classical waves across multiple dimensions [36], providing an important avenue for exploring various topological properties in acoustic, optic, and other classical systems.

The construction of 3D HOTIs typically requires either highly cumbersome coupling strengths or extremely complicated geometrical structures. Because of these complex structures, it is difficult to analyze the mechanism of topological phases when investigating the topological properties of materials [34, 37–39]. Based on the same configuration, theoretical research has proposed a new approach to achieve 3D TIs; it is related to the hierarchy of Dirac cones that correspond to the band structure of the topological phase transition [26]. Studies have shown that the topological phase transition caused by the lifting of the Dirac hierarchy is feasible and provides a method to realize HOTIs in 3D structures [27]. However, in contemporary studies, the hinge state was only observed along a single hinge, limiting the application of

hinge transport in multiple directions. In this study, we proposed a simple method to achieve Dirac hierarchy in 3D acoustic TIs with controllable topological phase transitions, allowing for hinge transport along three independent directions.

2. Dirac hierarchy in bulk and boundary

In this study, we presented a simple method to construct a 3D acoustic crystal with Dirac hierarchy. Compared to 3D HOTIs implemented by designing complex geometries or setting harsh coupling parameters, our method can use the same 3D basic configuration to peel off DCs in the bulk as well as boundary, achieving rich topological phase transitions and topological boundary states. As shown in figure 1(a), the basis vectors of the 3D acoustic honeycomb lattice were $a_1 = \left(\sqrt{3}/2, 1/2, 0\right) a$, $a_2 = \left(-\sqrt{3}/2, 1/2, 0\right) a$ and $a_3 = (0, 0, 1) H$, where a is the in-plane (xy-plane) lattice constant and H is the out-of-plane (z-direction) lattice constant. The unit cell was a bilayer graphene structure comprising several air resonators connecting the air plates shown in figure 1(b). The height of the cylindrical resonators was $L = 49.2$ mm, and the air plates with $h = 2.05$ mm connected the dispersed cylindrical resonators to form a rigid-bounded air resonant cavity that localized the sound wave. When the lattice constant $a = 168$ mm was three times the distance of the nearest adjacent cylindrical resonator $R = 56$ mm, and the radius of the cylindrical resonator in each layer was $r_1 = r_2 = 20$ mm, which was related to the interlayer coupling, an eight-fold bulk DC (figure 1(c)) appeared according to zone-folding effects, 3D bulk states were observed (figure 1(f)). When $r_1 > r_2$ ($r_1 = 21.6$ mm, $r_2 = 2$ mm), the strength of the interlayer coupling changed, and the mirror symmetry was broken; as a result, the eight-fold bulk DC split into double four-fold bulk DCs (left panel of figure 1(d)), creating the first-order topological bandgap. At this moment, the acoustic crystal underwent the topological phase transition, ensuring the emergence of the 2D surface DC in the bandgap (right panel of figure 1(d)) and the 2D topological surface state (figure 1(g)). Furthermore, the interlayer coupling was $r_1 = 10.8 r_2$ and $a = 168$ mm, we set $3R/a = 1.09$ to change the strength of the intralayer coupling; thus, we split the four-fold bulk DCs into double two-fold bulk Weyl and formed the second-order topological bandgap, which supported the existence of the 1D hinge DC (left panel of figure 1(e)), and it exhibited the topological 1D hinge state on the boundary of the 3D acoustical crystal (figure 1(h)). We focused on the two-fold bulk Weyl related to the split of four-fold bulk DC at lower frequencies.

According to the previous part, an eight-fold bulk DC (red dot) emerged at the Z point in the Brillouin zone, as shown in figure 2(a), and the degenerated node was $\sim$1.87 kHz, as $r_1 = r_2 = 20$ mm in the acoustic crystal. The acoustic eigenfields of the eight-fold degenerated node (insets in figure 2(a)) underlined the dipole p and quadrupole d nature, exhibiting the generation of dipole eigenstates accompanied by quadrupole eigenstates. However, the eight-fold bulk DC was broken and split into four-fold bulk DC pairs, symmetrically, forming a wide topological band gap in the range 1.66–2.18 kHz (gray region in figure 2(b)); this was because the strength of the interlayer coupling changed ($r_1 = 21.6$ mm, $r_2 = 2$ mm). As previously described, the four-fold bulk DC at lower frequencies was further transformed to double bulk Weyl, forming a bandgap (green region in figure 2(c)) by changing the strength of the intralayer coupling. To analyze the nature of the acoustic crystal, an effect tight-binding model was constructed, and its Hamiltonian was expressed as in equation (1)

$$H = I_2 \otimes H_{xy} + H_z \otimes I_6 \tag{1}$$

where I_N is an N-by-N identity matrix ($N = 2, 6$), and H_{xy} and H_z are the Hamiltonians for the in-plane monolayer honeycomb lattice and the out-of-plane SSH chain, respectively. Both these features block-off-diagonal forms in which $H_{xy} = \begin{bmatrix} 0 & Q \\ Q^\dagger & 0 \end{bmatrix}$ and $H_z = \begin{bmatrix} 0 & \rho \\ \rho^* & 0 \end{bmatrix}$, where Q and ρ are the couplings between different sublattices for the Kekulé honeycomb lattice (intralayer coupling) and SSH chain (interlayer coupling), respectively (supplemental material [40]). Since the matrix form of H_{xy} is similar to SSH chain, it can be considered as the extension of the 1D SSH model in xy-plane. Deducing equation (1), we determined that the eigenvalue of H was $E = E_z + E_{xy}$, with the corresponding eigenstate $\psi = \psi_z \otimes \psi_{xy}$, in which $E_{xy(z)}$ and $\psi_{xy(z)}$ are the eigenvalue and eigenstate, respectively, of $H_{xy}(H_z)$. Thus, if ψ_{xy} and ψ_z are both bulk states, then ψ is also a bulk state; if ψ_z is an edge state and ψ_{xy} is a bulk (edge) state, then ψ is a surface (hinge) state [26].

For a typical case, when the intralayer and interlayer coupling strengths were equal, the eight-fold bulk DC emerged (figure 2(d)). The first-order topological nature was considerably influenced by the interlayer coupling, which in turn depended on the strength of the intracell coupling s and intercell coupling t in the tight-binding model that was reduced to a classical 1D SSH model along the z-direction. As $s < t$, the 8-fold
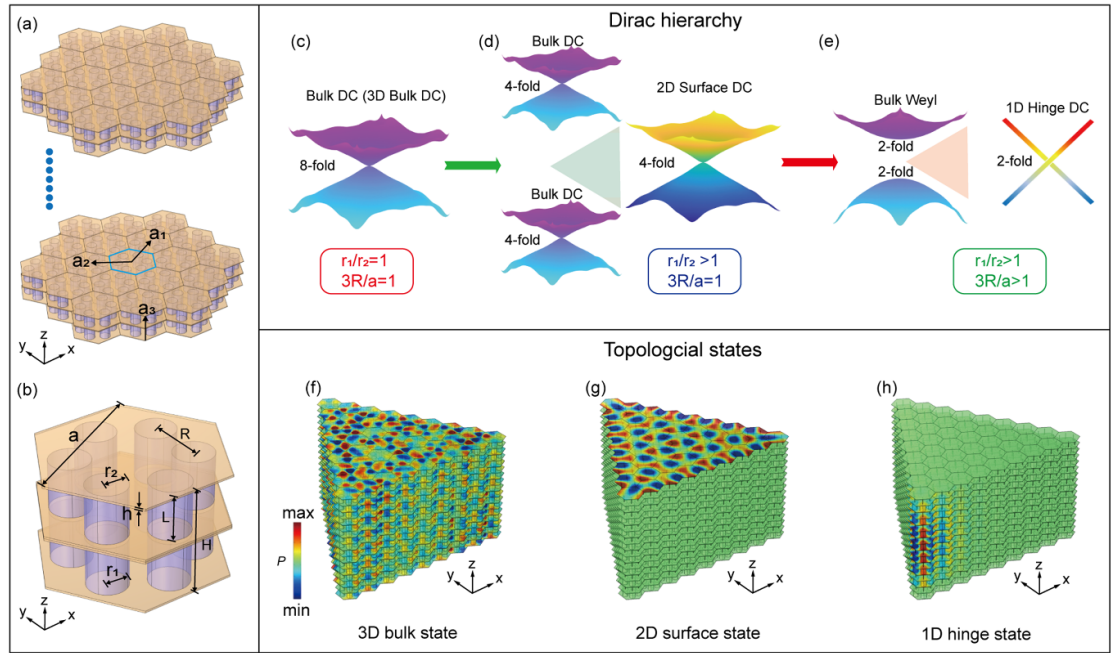
Figure 1. Dirac hierarchy in bulk and boundary. (a) Schematic diagram of the acoustic honeycomb lattice. (b) Unit cell of 3D acoustic crystal. (c)–(e) Dirac hierarchy including bulk and boundary state hierarchy. The eight-fold bulk DC split into two four-fold bulk DCs, and the bulk DC split into two bulk Weyl. Boundary Dirac hierarchy evolution from 3D bulk DC to 2D surface DC to 1D hinge DC (f)–(h) Topological states related to the corresponding Dirac hierarchy in (c)–(e).
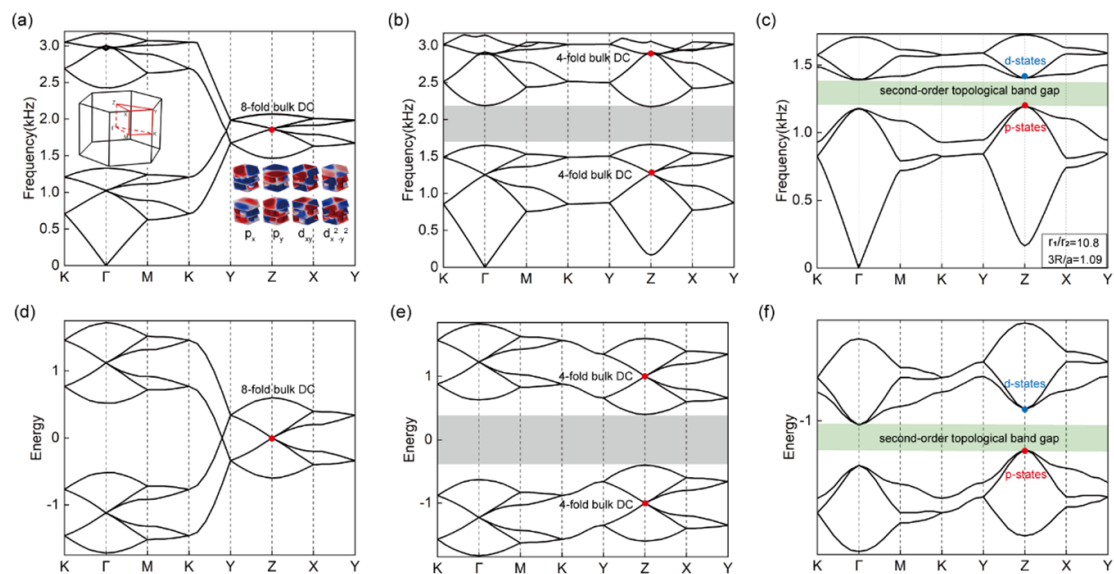

Figure 2. Band structure of Dirac hierarchy in acoustic crystal and tight-bounding model. (a) Bulk band dispersion at high-symmetry lines related to eight-fold bulk DC in acoustic crystal. Inset: Brillouin zones and eigenfields in the Dirac point with dipole p and quadrupole d nature. (b) Bulk band dispersion at high-symmetry lines related to four-fold bulk DCs in acoustic crystal and the first-order topological bandgap (gray region). (c) Bulk band dispersion at high-symmetry lines related to two-fold bulk Weyl at Z, and the second-order topological bandgap (green region). (d) Calculated band structures with equal intralayer and interlayer coupling strengths. (e) Calculated band structures with equal intralayer coupling strengths and unequal interlayer coupling strengths. Gray region: first-order topological bandgap. (f) Calculated band structures with unequal intralayer and interlayer coupling strengths. Green region: second-order topological bandgap.

bulk DC split into two 4-fold DCs (figure 2(e)), and the nontrivial Zak phase π was induced along the z-direction, which implied the emergence of the 2D topological surface states (2D boundary Dirac hierarchy) in the topological bandgap protected by inversion symmetry [41–43]. The second-order topological nature was considerably influenced by the intralayer coupling, and the tight-binding model can be regarded as the extension of the 1D SSH model in xy-plane. Under the interlayer coupling of $s < t$, when $w < v$ (intracell
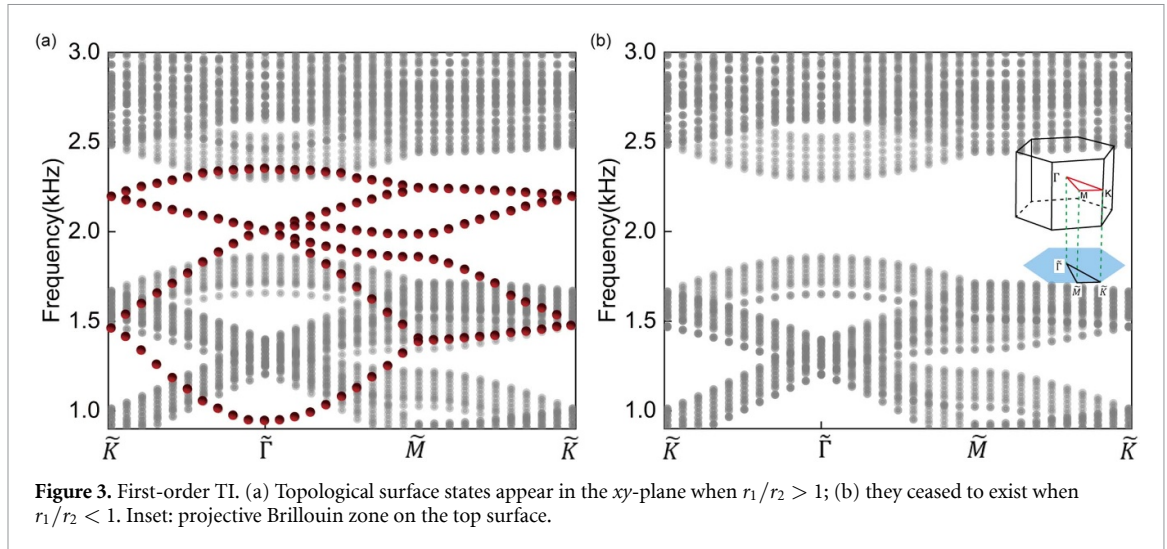
Figure 3. First-order TI. (a) Topological surface states appear in the *xy*-plane when $r_1/r_2 > 1$; (b) they ceased to exist when $r_1/r_2 < 1$. Inset: projective Brillouin zone on the top surface.

coupling *w* and intercell coupling *v* along the *xy*-plane), the four-fold bulk DC at the lower frequency transformed to double two-fold DCs (figure 2(f)).

3. First-order 3D acoustic TI

Further, we computed the projected surface dispersion along the high-symmetry line $\tilde{K} - \tilde{\Gamma} - \tilde{M} - \tilde{K}$ (the projections of the high-symmetry points on the *xy*-plane) of a truncated honeycomb first-order TI with ten layers stacked along the *z*-direction. We distinguished between two cases, that is, figures 3(a) and (b) represent interlayer couplings with $r_1/r_2 > 1$ and $r_1/r_2 < 1$, respectively. Topological surface states spanned the frequency range of the bulk band gap with a gapless four-fold DC when $r_1/r_2 > 1$, while they ceased to exist when $r_1/r_2 < 1$ (red spheres: four-fold surface DC; gray dots: bulk state).

The topological nature of the first 3D acoustic crystal was as follows. According to equation (1), the lattice configuration of the first sample indicated that H_{xy} had a gapless eigenspectrum, and ψ_{xy} was a bulk state, while H_z had a topological edge state ψ_z because the winding number

$$w_z = -\frac{1}{2\pi} \int_0^{2\pi} \frac{d}{dk_z} \arg\left(\det \rho\right) dk_z \qquad (2)$$

was nonzero [26]. Consequently, $\psi = \psi_z \otimes \psi_{xy}$ appeared to be 2D topological surface states.

4. Second-order 3D acoustic TI

In section 2, we discussed the theoretical Dirac hierarchy in bulk as well as boundary. Herein, we investigated the higher-order topological characteristics of 3D acoustic TIs. When $r_1/r_2 = 10.8$ and $3R/a = 1.09$, two 2-fold degenerated nodes appeared at *Z*, which were attributed to the modes of *d*- and *p*-states, and they shaped the second-order topological bandgap (figure 4(a)). The eigenmodes of the unit cell at *Z* exhibited a pair of pseudospin dipolar states above the bandgap, which were even or odd symmetrical to the *x/y* axes, and they were similar to the p_x/p_y-type orbitals (inset in figure 4(a)). In contrast, a pair of pseudospin quadrupolar states appeared below the bandgap, which showed the odd symmetry on the *x*- and *y*-axes corresponding to the d_{xy}-type orbital, or even symmetry on the *x*- and *y*-axes corresponding to the $d_{x^2-y^2}$-type orbital (inset in figure 4(a)). We first maintained the interlayer coupling r_1/r_2 and altered the intralayer coupling $3R/a$ and then transformed the degenerated nodes from two-fold to four-fold to two-fold, achieving the closing and reopening of the bandgap (figure 4(b)). The corresponding acoustic eigenmodes at *Z* were also reversed; figures 4(b) and (c) illustrate the inversion process. When $3R/a < 1$, the acoustic TI was trivial; while at $3R/a > 1$, it was nontrivial and exhibited second-order topology.

The 3D second-order TI enabled the existence of 1D hinge states in the bandgap, and the acoustic fields were localized at the hinge of the system. We considered the realization of hinge states on the out-of-plane (*z*-direction) and in-plane (*xy*-plane) in acoustic TIs. First, we discussed the method for achieving the out-of-plane hinge state. The triangular supercell structure was constructed, which comprised nontrivial unit cells arranged in the *xy*-plane. The side length of the equilateral triangle was 9*a*, and the *z*-direction was
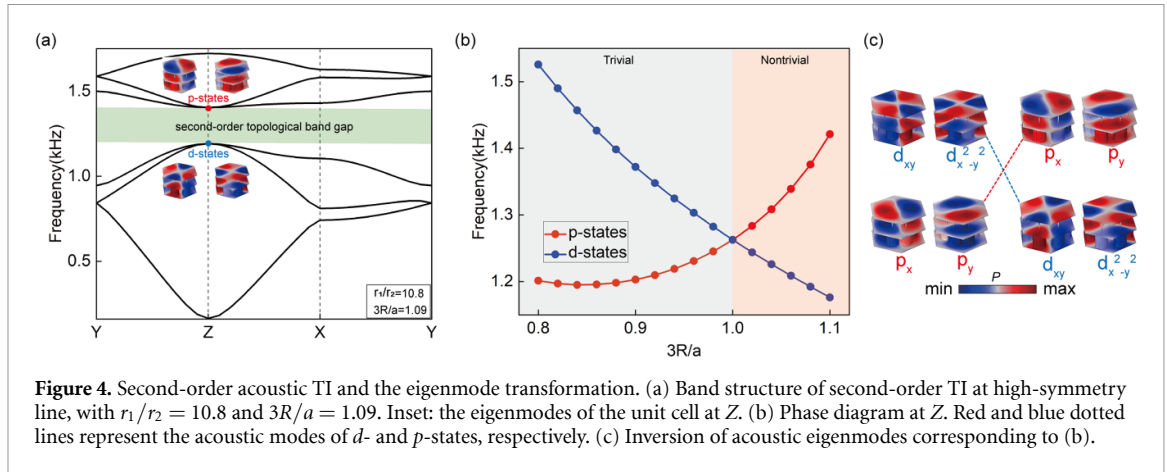
Figure 4. Second-order acoustic TI and the eigenmode transformation. (a) Band structure of second-order TI at high-symmetry line, with $r_1/r_2 = 10.8$ and $3R/a = 1.09$. Inset: the eigenmodes of the unit cell at Z. (b) Phase diagram at Z. Red and blue dotted lines represent the acoustic modes of d- and p-states, respectively. (c) Inversion of acoustic eigenmodes corresponding to (b).

set to periodic, as shown in figure 5(b). Figure 5(a) exhibits the numerical projected dispersion along k_z, and the gapped hinge states appear at frequencies of 1.28–1.30 kHz, which was under the bandgap range. The acoustic pressure field distributions of bulk and hinge states are shown in figures 5(b) and (c), respectively. Clearly, the acoustic energy was highly localized at the corner of the air cavity of the acoustic supercell, that is, the acoustic energy was concentrated on the 1D hinge along the z-direction, and the bulk state was dispersed throughout the system. Second, we discussed the existence of the hinge state in the in-plane. As shown in figure 5(e), the 3D acoustic ribbon-shaped supercell comprised 216 trivial unit cells and 234 nontrivial unit cells. Periodic boundary conditions were applied on both sides of the supercell along the y-direction. The numerical projected dispersion along the k_y direction is shown in figure 5(d), which reveals that gapped 1D hinge Dirac hierarchy (red curves) were achieved. The simulated acoustic pressure field distribution of the surface and hinge states at $k_y = 0$ corresponding to the blue star in the gray area of figure 5(d) are shown in figures 5(e) and (f). The surface states of acoustic energy were highly localized at the interface of the trivial and nontrivial parts (yz-plane) (figure 5(e)). However, the acoustic energy of the 1D hinge states was only distributed along the y-direction (figure 5(f)).
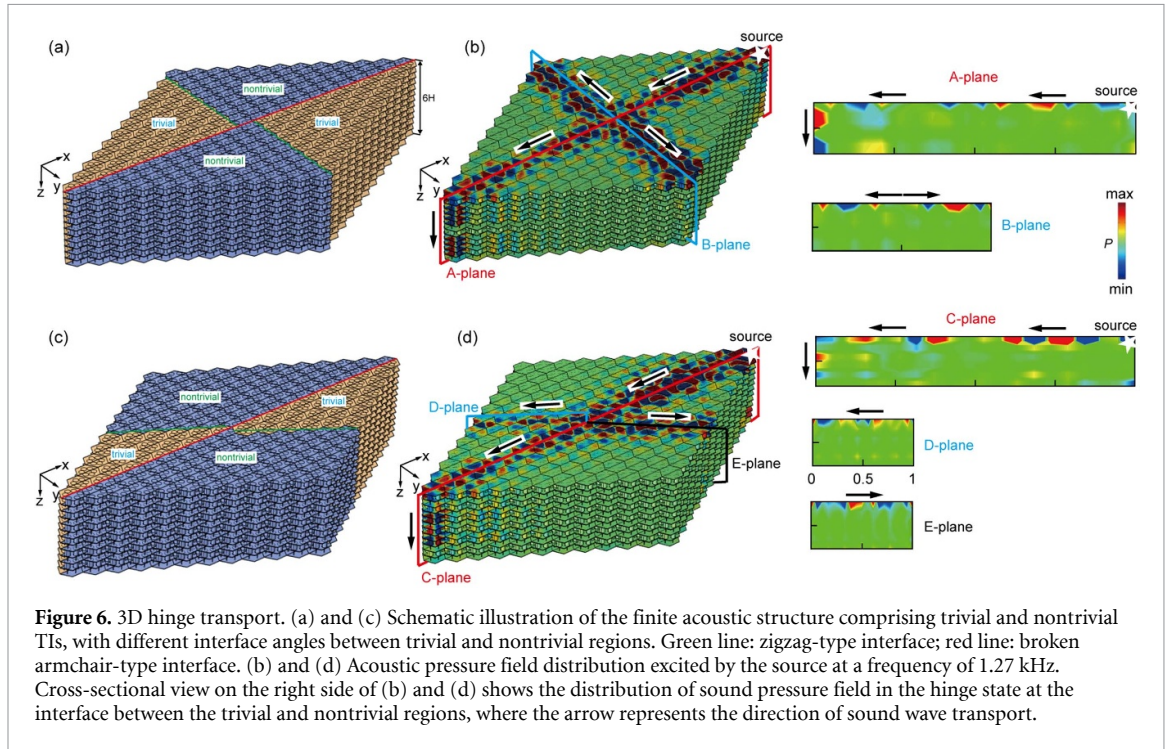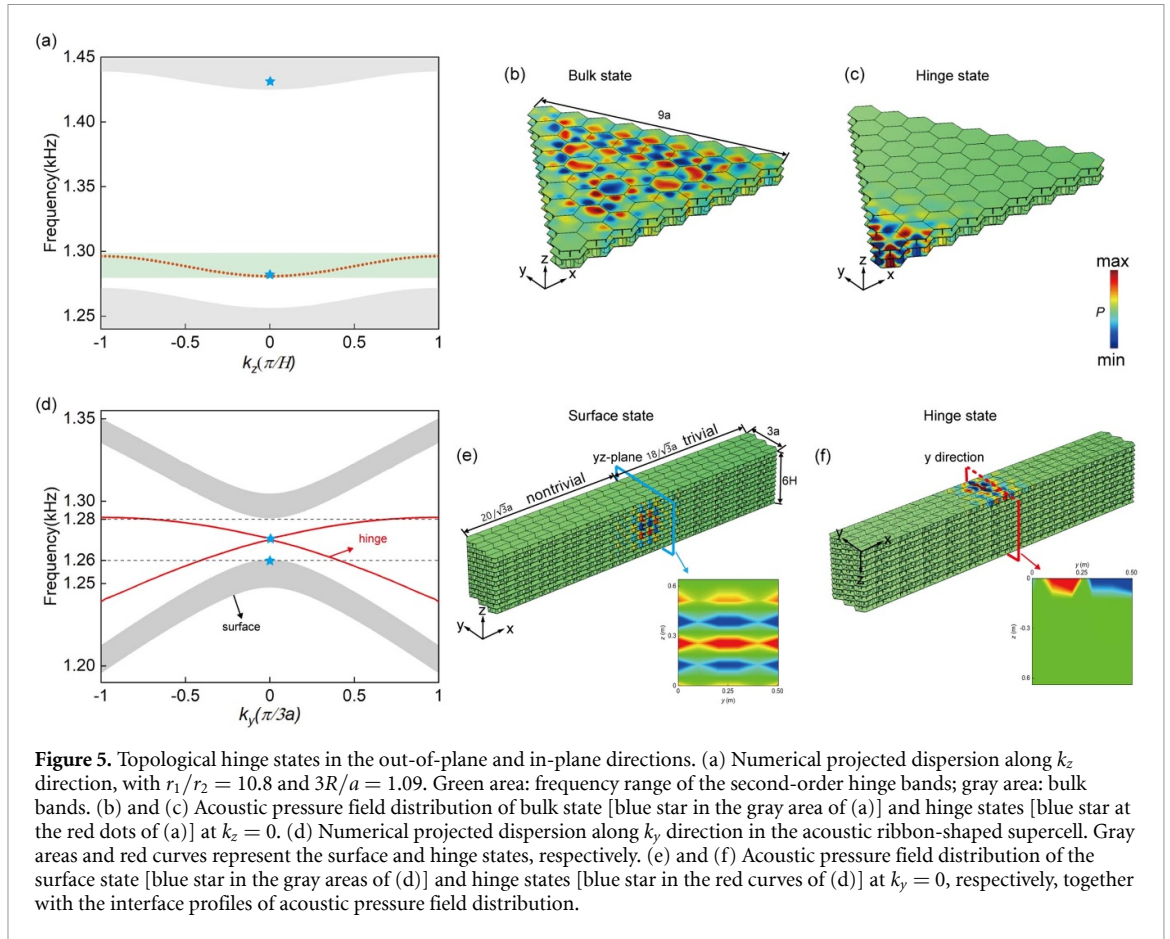
The emergence of these hinge states was ascribed to a net-winding number when considering a specific lattice termination [26]. An alternative explanation was obtained by considering the mirror symmetry M_y along the perpendicular direction of the molecule-zigzag hinge and by calculating the mirror winding numbers. Since M_y commutes with H_{xy} at Γ point, the off-diagonal block Q can be block-diagonalized into two sectors $Q^{\pm}$, associated with the $+1$ and -1 eigenvalues of M_y [44]. This further allowed us to calculate the winding numbers in each sector separately using equation (3)

$$w_{MZ}^{\pm} = -\frac{1}{2\pi} \int_0^{2\pi} \frac{d}{dk_{\perp}} \arg\left(\det Q^{\pm}\right) dk_{\perp} \tag{3}$$

where the subscript denotes the molecule-zigzag edge, and $k_{\perp}$ is the wave vector along the perpendicular direction of the edge. According to the calculated results, $w_{MZ}^{\pm} = 0$ for $w > v$, while $w_{MZ}^{\pm} = \mp 1$ for $w < v$, which corresponds to the two helical hinge states in our case [40]. Moreover, because of the mirror symmetry M_y, these two helical hinge states degenerate at $k_y = 0$ [44], forming a 1D gapless hinge DC within the surface band gap.

5. Hinge transport

In section 4, the hinge states along the z-direction and xy-plane were realized independently. Hence, the natural next question is whether the hinge states exist simultaneously along all three independent directions in the HOTIs. A finite 3D acoustic structure spliced together from trivial and nontrivial insulators was designed to explore hinge transport in the three independent directions. As shown in figure 6(a), the domain walls between trivial and nontrivial regions were orthogonal; the green and red lines denote the zigzag-type and broken armchair-type domain walls, respectively. The zigzag-type interface was parallel to the y-direction and all the unit cells remained intact. In contrast, the broken armchair-type interface was arranged along the x-direction and the unit cells near the interface were cut in half. An excitation source with a frequency of 1.27 kHz (white star in figure 6(b)) was placed on the top surface of the finite 3D acoustic insulator. The simulated acoustic pressure field distribution exhibited higher-order topology, and the acoustic energy was efficiently transported along the hinges in three independent directions (figure 6(b)).

Figure 5. Topological hinge states in the out-of-plane and in-plane directions. (a) Numerical projected dispersion along k_z direction, with $r_1/r_2 = 10.8$ and $3R/a = 1.09$. Green area: frequency range of the second-order hinge bands; gray area: bulk bands. (b) and (c) Acoustic pressure field distribution of bulk state [blue star in the gray area of (a)] and hinge states [blue star at the red dots of (a)] at $k_z = 0$. (d) Numerical projected dispersion along k_y direction in the acoustic ribbon-shaped supercell. Gray areas and red curves represent the surface and hinge states, respectively. (e) and (f) Acoustic pressure field distribution of the surface state [blue star in the gray areas of (d)] and hinge states [blue star in the red curves of (d)] at $k_y = 0$, respectively, together with the interface profiles of acoustic pressure field distribution.

Figure 6. 3D hinge transport. (a) and (c) Schematic illustration of the finite acoustic structure comprising trivial and nontrivial TIs, with different interface angles between trivial and nontrivial regions. Green line: zigzag-type interface; red line: broken armchair-type interface. (b) and (d) Acoustic pressure field distribution excited by the source at a frequency of 1.27 kHz. Cross-sectional view on the right side of (b) and (d) shows the distribution of sound pressure field in the hinge state at the interface between the trivial and nontrivial regions, where the arrow represents the direction of sound wave transport.

Thereafter, we changed the interface angle of the trivial and nontrivial regions (figure 6(c)) and placed an excitation source with a frequency of 1.27 kHz at the same location (white star in figure 6(d)). As expected, acoustic energy was transport along the interface, successfully achieving 3D hinge transport (figure 6(d)). This finding enables us to design an expected interface to realize flexible transport.

6. Conclusion

In this study, we realized Dirac hierarchy in bulk and boundary using the same basic configuration that is used in acoustic crystals. We broke the symmetry of the 3D acoustic structure step-by-step and realized the 2D surface DC with unequal interlayer coupling strengths and equal intralayer coupling strengths. We achieved the 1D hinge DC with unequal interlayer and intralayer coupling strengths. In particular, hinge states were observed along the three independent directions in the 3D HOTIs, successfully achieving the controllable transport of acoustic waves at the hinges. The findings of our study provide a versatile platform for exploring controllable topological phase transitions, different dimensional Dirac hierarchies, and also provides a new idea for designing acoustic devices with flexible 3D hinge transports. We expect that the work can be extended to other classical wave systems by regulating interlayer and intralayer coupling strengths based on this simple 3D structure, and it can greatly enrich the content of higher-order topological states, which can be of great significance for the controllable transport of optical, acoustic, and elastic waves in 3D structures.

Data availability statement

The data cannot be made publicly available upon publication because no suitable repository exists for hosting data in this field of study. The data that support the findings of this study are available upon reasonable request from the authors.

Acknowledgments

References

[1] Hasan M Z and Kane C L 2010 *Rev. Mod. Phys.* **82** 3045
[2] Qi X and Zhang S 2010 *Phys. Today* **63** 33
[3] Qi X and Zhang S 2011 *Rev. Mod. Phys.* **83** 1057
[4] Shen S 2014 *Natl Sci. Rev.* **1** 49
[5] Zhou Y, Bandaru P R and Sievenpiper D F 2018 *New J. Phys.* **20** 123011
[6] Yang Z, Gao F, Shi X, Lin X, Gao Z, Chong Y and Zhang B 2015 *Phys. Rev. Lett.* **114** 114301
[7] Lu J, Qiu C, Deng W, Huang X, Li F, Zhang F, Chen S and Liu Z 2018 *Phys. Rev. Lett.* **120** 116802
[8] Fleury R, Khanikaev A B and Alu A 2016 *Nat. Commun.* **7** 11744
[9] Yves S, Fleury R, Lemoult F, Fink M and Lerosey G 2017 *New J. Phys.* **19** 075003
[10] Ding Y, Peng Y, Zhu Y, Fan X, Yang J, Liang B, Zhu X, Wan X and Cheng J 2019 *Phys. Rev. Lett.* **122** 014302
[11] Geng Z, Peng Y, Li P, Shen Y, Zhao D and Zhu X 2019 *J. Phys.: Condens. Matter* **31** 245403
[12] Zhang K, Zhang X, Wang L, Zhao D, Wu F, Yao Y, Xia M and Guo Y 2021 *J. Appl. Phys.* **130** 064502
[13] Jia D, Sun H, Xia J, Yuan S, Liu X and Zhang C 2018 *New J. Phys.* **20** 093027
[14] Deng Y, Ge H, Tian Y, Lu M and Jing Y 2017 *Phys. Rev. B* **96** 184305
[15] Ma G, Xiao M and Chan C 2019 *Nat. Rev. Phys.* **1** 281
[16] Ezawa M 2018 *Phys. Rev. Lett.* **120** 026801
[17] Langbehn J, Peng Y, Trifunovic L, von Oppen F and Brouwer P W 2017 *Phys. Rev. Lett.* **119** 246401
[18] Khalaf E 2018 *Phys. Rev. B* **97** 205136
[19] Schindler F, Cook A M, Vergniory M G, Wang Z J, Parkin S S P, Bernevig B A and Neupert T 2018 *Sci. Adv.* **4** eaat0346
[20] Benalcazar W A, Bernevig B A and Hughes T L 2017 *Phys. Rev. B* **96** 245115
[21] Zhang F, Kane C L and Mele E J 2013 *Phys. Rev. Lett.* **110** 046404
[22] Song Z, Fang Z and Fang C 2017 *Phys. Rev. Lett.* **119** 246402
[23] Roy B 2019 *Phys. Rev. Res.* **1** 032048(R)
[24] Benalcazar W A, Bernevig B A and Hughes T L 2017 *Science* **357** 61
[25] Calugaru D, Juricic V and Roy B 2019 *Phys. Rev. B* **99** 041301(R
[26] Zheng L and Christensen J 2021 *Phys. Rev. Lett.* **127** 156401
[27] Yang L *et al* 2022 *Phys. Rev. Lett.* **129** 125502
[28] Luo L, Wang H, Lin Z, Jiang B, Wu Y, Li F and Jiang J 2021 *Nat. Mater.* **20** 794
[29] Wei Q, Zhang X, Deng W, Lu J, Huang X, Yan M, Chen G, Liu Z and Jia S 2021 *Phys. Rev. Lett.* **127** 255501
[30] Xue H, Ge Y, Sun H, Wang Q, Jia D, Guan Y, Yuan S, Chong Y and Zhang B 2020 *Nat. Commun.* **11** 2442
[31] He C, Lai H, He B, Yu S, Xu X, Lu M and Chen Y 2020 *Nat. Commun.* **11** 2318
[32] Xu C, Chen Z, Zhang G, Ma G and Wu Y 2021 *Sci. Bull.* **66** 1740
[33] Zhang X, Wang H, Lin Z, Tian Y, Xie B, Lu M, Chen Y and Jiang J 2019 *Nat. Phys.* **15** 582
[34] Xue H, Yang Y, Liu G, Gao F, Chong Y and Zhang B 2019 *Phys. Rev. Lett.* **122** 244301
[35] Geng Z, Peng Y, Lv H, Xiong Z, Chen Z and Zhu X 2022 *J. Phys.: Condens. Matter* **34** 104001

[36] Mousavi S H, Khanikaev A B and Wang Z 2015 *Nat. Commun.* **6** 8682
[37] Zhang X, Xie B, Wang H, Xu X, Tian Y, Jiang J, Lu M and Chen Y 2019 *Nat. Commun.* **10** 5331
[38] Weiner M, Ni X, Li M, Alu A and Khanikaev A B 2020 *Sci. Adv.* **6** eaay4166
[39] Qi Y, Qiu C, Xiao M, He H, Ke M and Liu Z 2020 *Phys. Rev. Lett.* **124** 206601
[40] See supplemental material for the theoretical details and derivation of the winding numbers.
[41] Yan M, Huang X, Luo L, Lu J, Deng W and Liu Z 2020 *Phys. Rev.* B **102** 180102(R
[42] Zak J 1989 *Phys. Rev. Lett.* **62** 2747
[43] Atala M, Aidelsburger M, Barreiro J T, Abanin D, Kitagawa T, Demler E and Bloch I 2013 *Nat. Phys.* **9** 795
[44] Noh J, Benalcazar W A, Huang S, Collins M J, Chen K P, Hughes T L and Rechtsman M C 2018 *Nat. Photon.* **12** 408